# DECONVOLUTION FOR IMPROVED MULTIFRACTAL CHARACTERIZATION OF TISSUES IN ULTRASOUND IMAGING

*Herwig Wendt, Mohamad Hourani, Adrian Basarab, Denis Kouamé*

IRIT, CNRS UMR 5505, University of Toulouse, Toulouse, France.

{wendt, hourani, basarab, kouame}@irit.fr

## ABSTRACT

Several existing studies showed the interest of estimating the multifractal properties of tissues in ultrasound (US) imaging. However, US images are not carrying information only about the tissues, but also about the US scanner. Deconvolution methods are a common way to restore the tissue reflectivity function, but, to our knowledge, their impact on estimated fractal or multifractal behavior has not been studied yet. The objective of this paper is to investigate this influence through a dedicated simulation pipeline and an *in vivo* experiment.

***Index Terms*—** Ultrasound imaging, multifractal analysis, tissue characterization

## 1. INTRODUCTION

Ultrasonics tissue characterization (UTC) is an area of intensive research, aiming at complementing the visual observation of ultrasound (US) images with quantitative information about the tissues. Such quantitative measurements, very useful in computer-aided screening tools, are generally extracted from US images such as beamformed radiofrequency (RF), envelope, computed by demodulation of individual RF signal, or B-mode, log-compressed envelope, images. The most used parameters to characterize the tissues rely on acoustical properties (e.g., attenuation, speed of sound, backscattering coefficient [1]) or statistical and spectral information (e.g., [2]). In addition, several studies showed the interest of extracting from US images fractal or multifractal parameters, potentially related to the fractal or multifractal behavior of tissues in space and time (e.g., [3]). However, the good agreement between the parameters computed from the US images and those specific to the tissues' signature is difficult to be proven in practice, thus mitigating the confidence one can have in such measurements. In our previous study in [4], we proposed a simulation pipeline that generated US RF images from tissue reflectivity functions (TRF) with available ground truth of tissue multifractal characteristics. Multifractal spectra were further estimated from the resulting simulated images (RF, envelope and B-mode images were considered) using the algorithm in [5, 6] and compared with the ground truth. The results in [4] led to the conclusion that only part of the multifractal characteristics were preserved in US (RF and envelope) images, but B-mode images bear no multifractal ressemblance with simulated tissues.

The main objective herein is to study the impact of deconvolution on the multifractal analysis of US images. The features used in UTC, independently on their acoustic, statistic, spectral or multifractal nature, are computed directly on acquired echo data (RF, envelope or B-mode images). Nevertheless, this data is not perfectly representative of the tissues, but also carries information about the US scanner, through its point spread function (PSF). Therefore, the restoration of TRF from US images is a subject of active research. Existing algorithms are assuming that RF images from soft tissues can be modeled as the convolution between the TRF and the PSF (e.g., [7, 8]). They aim at restoring the TRF by inverting this model, using various image regularizations, among which the $\ell_1$-norm is a common choice also used in this work. The impact of deconvolution in UTC was already evaluated in [7] for statistical parameters, but, to the best of our knowledge, has not been studied yet for multifractal features.

Moreover, to also study purely fractal (Hurst) parameters, we make use here of a more versatile simulation pipeline in which fractional Gaussian noise substitutes the independent Gaussian scatter amplitudes of [4]. The estimated multifractal spectra from restored TRF are shown to be in better agreement with the ones of the simulated tissues, compared to those extracted from RF or envelope images. Following the results in [4], the B-mode images were not considered in this study given their low correlation with the tissues from a multifractal viewpoint. Finally, we compare the simulation results to those obtained on a real-world US image of thyroid.

The remainder of this paper is organized as follows. Section 2 provides a brief summary on US image deconvolution and multifractal analysis. Section 3 details the US simulation procedure used to generate images from tissues with available multifractal ground truth. The results are regrouped in Section 4, and conclusion and perspectives are drawn in Section 5.

Work supported by Grant ANR-18-CE45-0007 MUTATION.

## 2. MULTIFRACTAL ANALYSIS AND IMAGE DECONVOLUTION

### 2.1. US image deconvolution

Under the hypothesis of soft tissue examination and using the first order Born approximation, observed RF images after beamforming can be related to the unknown TRF by a linear model, namely a two-dimensional convolution with the system PSF

$$\boldsymbol{y} = \boldsymbol{H}\boldsymbol{x} + \boldsymbol{n}, \tag{1}$$

where $\boldsymbol{y}$ is the beamformed RF image, $\boldsymbol{x}$ is the TRF to be estimated and $\boldsymbol{n}$ is the measurement noise supposed white independent Gaussian. The RF image, the TRF and the noise are all expressed in the standard vectorized version. $\boldsymbol{H}$ is a square matrix accounting for 2D block circulant matrices with circulant blocks and thus easily tractable in practice. Estimating $\boldsymbol{x}$ from $\boldsymbol{y}$ is a typical deconvolution problem. A standard way to solve it is to estimate $\boldsymbol{x}$ by minimizing a cost function, see (2), consisting of a data fidelity term (an $\ell_2$-norm here due to the Gaussianity of the noise) and a regularizer. In this work, an $\ell_1$-norm is used to regularize the estimated TRF, due to its popularity in US image deconvolution.

$$\min_{\boldsymbol{x}} \frac{1}{2}\|\boldsymbol{y} - \boldsymbol{H}\boldsymbol{x}\|_2^2 + \mu\|\boldsymbol{x}\|_1, \tag{2}$$

where $\mu$ is a hyperparameter balancing the weight of the two terms. To solve (2), we use an alternating direction method of multipliers (ADMM) based optimization algorithm [9].

### 2.2. Multifractal analysis

We briefly recall the key concepts of multifractal analysis, see, e.g., [5, 6] for details.

**Multifractal spectrum.** Multifractal analysis characterizes texture in an image $F(\mathbf{x})$ by its *multifractal spectrum* $\mathcal{D}(h)$, defined as the Hausdorff dimension of the sets of points $\mathbf{x}$ with same pointwise regularity index $h(\mathbf{x}) = h$, where smaller (larger) $h(\mathbf{x})$ correspond with rougher (smoother) $F(\mathbf{x})$. The spectrum $\mathcal{D}(h)$ can be approximated as

$$\mathcal{D}(h) \approx 2 + (h - c_1)^2/(2c_2) \tag{3}$$

where the coefficient $c_1$ quantifies the *average* regularity of $F$ that accounts for its self-similarity or *fractality*, and $c_2 \leq 0$ quantifies the *fluctuations* of regularity and accounts for *multifractality* [6]. In practice, multifractal analysis amounts to estimating $\mathcal{D}(h)$ or the parameters $c_1$ and $c_2$ in approximation (3). Fig. 1 provides illustrations for multifractal textures with different (multi)fractal parameters $c_1, c_2$.

**Multifractal formalism.** The estimation of $\mathcal{D}(h)$ relies on the *wavelet leaders*. They are defined as the largest discrete wavelet transform coefficients $d_F^{(m)}(j, \boldsymbol{k})$ of $F$ (cf. [10]), across all finer scales and within a small spatial neighborhood, $\ell(j, \boldsymbol{k}) = \sup_{m\in(1,2,3),\lambda'\subset 3\lambda_{j,\boldsymbol{k}}} |d_F^{(m)}(\lambda')|$, where $\lambda_{j,\boldsymbol{k}}$ is the dyadic cube of side length $2^j$ centered at $\boldsymbol{k}2^j$ and $3\lambda_{j,\boldsymbol{k}} = \bigcup_{n_1,n_2=\{-1,0,1\}} \lambda_{j,k_1+n_1,k_2+n_2}$ the union with its eight neighbors, see [6] for details.

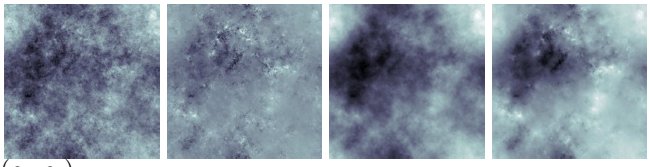

$(c_1, c_2) =$ $(0.3, -0.01)$ $(0.3, -0.1)$ $(0.7, -0.01)$ $(0.7, -0.1)$

**Fig. 1**. **Synthetic multifractal images.** Realizations of multifractal random walk for different values for $c_1$ and $c_2$.

It can be shown that the cumulants of order $p \geq 1$, $C_p(j) = \mathrm{Cum}_p(\ln \ell(j, k))$, of the log-leaders $\ln \ell(j, k)$ of $F$ behave as $C_p(j) = c_p^0 + c_p \ln 2^j$. This can be used to define simple and robust estimators for the parameters $c_1$ and $c_2$ of $\mathcal{D}(h)$ in (3) by means of linear regressions of the average and sample variance of $\ln \ell(j, k)$ as functions of $\ln 2^j$ [5, 6].

## 3. US IMAGE SIMULATION

To investigate the relationship between the multifractal parameters of a tissue and those that are estimated for the resulting simulated image, we follow the standard simulation strategy used in the US literature and replace the TRF with synthetic realizations of a stochastic process with known multifractal properties controlled by $(c_1, c_2)$. The parameters $c_1, c_2$ are then estimated for each image independently. Example images corresponding with the different stages of the pipeline are sketched in Fig. 2.

**Multifractal TRF (trf).** We generate a TRF that mimics the scattering map with prescribed multifractal properties. To this end, we numerically synthesize TRFs as realizations of multifractal random walk (MRW), whose multifractal spectrum is given by $\mathcal{D}(h) = 2 + (h - c_1)^2/(2c_2)$, see [11, 12] for details. Its construction matches the standard US simulation strategy according to which scatterers are modeled as independent Gaussian random variables whose variances encode local reflectivity; for MRW, a multifractal cascade (controlled by $c_2$) modulates the local variance of fractional Gaussian noise (with Hurst parameter $H = c_1 + c_2$). We simulate regularly sampled TRF. It has been checked that this leads to equivalent results as drawing scatterer positions at random from a uniform distribution in the field of view, with subsequent interpolation to a regular grid, and yields speckle characteristics close to those observed in practice.

**RF signal (rf).** Next, the TRF is convolved with a realistic PSF generated with Field II simulator [13], resulting into an RF image.

**Envelope (env).** The RF image is further axially demodulated, resulting into an envelope image.

**Deconvolution (dec).** Alternatively, deconvolution is performed as described in Section 2.1, assuming perfect knowl-

edge of the PSF.

**Enveloped of deconvolved image (env(dec)).** Finally, we also compute the envelope of the image obtained by deconvolution, to remove possible residual reverberation.

## 4. RESULTS

### 4.1. Simulation results

Collections of MRW images with various multifractal parameters were simulated as described above. The value for the fractal parameter was set to $c_1 \in (0.1, 0.2, \ldots, 0.9)$, and for the multifractality parameter to $c_2 \in (-0.1, -0.09, \ldots, -0.01, 0)$, covering a large range of realistic multifractal properties. For each combination $(c_1, c_2)$, 100 independent realizations of MRW of size $512 \times 512$ were synthesized and used in the simulation pipeline. The parameters $c_1$ and $c_2$ were estimated for the trf, rf, env, dec and env(dec) images, respectively, as detailed in Section 2, using Daubechies2 wavelets and scales $j \in (4, 6)$ for linear regressions; values reported for $c_1$ correspond to the primitive of the image.

**Scale invariance.** Fig. 3 (left column) plots average cumulants $C_1(j)$ and $C_2(j)$ as a function of $j$. It shows that those obtained for the rf and env images strongly differs from that of the trf image, for $C_1(j)$ for all scales, and for $C_2(j)$ for the fine scales. In contrast, the deconvolution effectively restores the linear behavior across scales for all scales for $C_1(j)$, and for all but the finest scales for $C_2(j)$.

**(Multi)fractal parameters $c_1$ and $c_2$.** Fig. 3 (right column) plots average estimates for $c_1$ (top) and $c_2$ (bottom) as a function of the prescribed values $c_1$ resp. $c_2$. Results are consistent with those of the previous paragraph. The images rf, dec and env(dec) produce estimates for the fractal parameter $c_1$ that are strongly biased and follow the tendency of the prescribed $c_1$ values at best very weakly. In contrast, the estimates for $c_1$ obtained after deconvolution tightly reproduce the prescribed values. For the multifractal parameter $c_2$, all images enable a reasonably accurate assessment of the value prescribed to the TRF. The best average estimates for $c_2$ are also obtained after deconvolution.

**Quantitative analysis.** Tab. 1 reports the correlation coefficient $\rho$, bias and root mean squared error (rmse) of the estimates obtained for rf, env, dec and env(dec) images, respectively, computed w.r.t. estimates obtained for the trf reference image. It confirms that the estimates for $c_1$ and $c_2$ after deconvolution are strongly correlated with those of the TRF model ($\rho \geq 0.98$), unlike those for the other images, and produce significantly smaller rmse values (e.g., up to 2 orders of magnitude smaller than those of rf for $c_1$). It also shows that computing envelopes strongly deteriorates multifractal parameter estimates, even after deconvolution.

Overall, this simulation study leads to conclude that only estimates obtained after deconvolution accurately reproduce the full set of fractal and multifractal properties of the TRF.

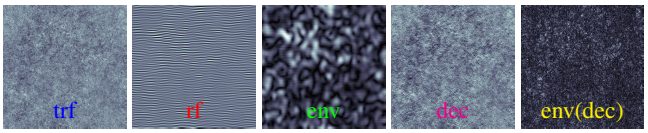


**Fig. 2. Simulation pipeline.** Synthetic images at different steps of the simulation pipeline, illustrating that deconvolution recovers a large part of visual details of the original trf.

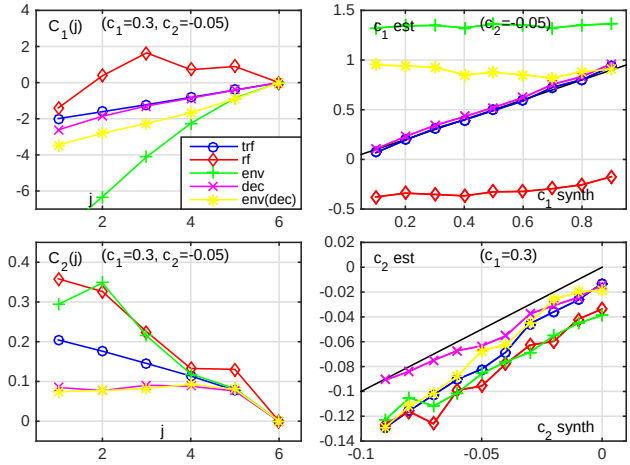


**Fig. 3. Log-cumulants and estimation for simulated data.** Average estimates $C_1(j)$, $C_2(j)$ and $c_1$, $c_2$.

### 4.2. Illustration for experimental data

We complement the simulation study with a result on an *in vivo* thyroid image acquired from a healthy subject, plotted in Fig. 4(a). Multifractal spectra were estimated for two image patches extracted at the same depth and from different tissues. The patches were interpolated to isotropic axial and lateral pixel resolution of $\approx 0.02$ mm to match the simulation. In this experiment, only the US modes were available. These four pairs of images (two patches for rf, env, dec, env(dec)) are plotted in Fig. 4(b-e), with estimates for $c_1$, $c_2$. The deconvolution problem is more difficult here than in the simulation because the PSF is unknown and can vary in space, resulting in clearly visible reverberation artifacts (cf. Fig. 4(d)). We observe that the estimates for multifractality $c_2$ are largely consistent across the images, corroborating the simulation results as well as those reported in [4], where changes in $c_2$ of US images were found to indicate a change in multifractality for the tissues. As far as the fractal parameter $c_1$ is concerned, the values for the rf and dec images are very similar and close to the values observed for rf in the simulation study. This suggests that the deconvolution has not been successfully unveiling the fractality of the tissue, likely due to the reverberation artifacts caused by a bad estimation of the PSF phase. One could study the envelope of the images in an attempt to remove the residual oscillations, yet this strongly alters the parameter $c_1$, as already observed for the simula-

| $c_1$ | rf | env | dec | env(dec) |
|---|---|---|---|---|
| $\rho$ | 0.46 | 0.21 | **1.00** | 0.38 |
| bias | $-1.022$ | 0.628 | **0.032** | 0.090 |
| rmse | 1.037 | 0.668 | **0.034** | 0.258 |
| $c_2$ | rf | env | dec | env(dec) |
| $\rho$ | 0.63 | 0.47 | **0.98** | 0.60 |
| bias | $-0.007$ | $-0.010$ | 0.010 | $\mathbf{-0.003}$ |
| rmse | 0.046 | 0.058 | **0.016** | 0.053 |

**Table 1**. Correlation coefficient $\rho$, bias and rmse of estimates for $c_1$ (top) and $c_2$ (bottom) calculated w.r.t. the estimates obtained for the trf image (best results marked in bold).

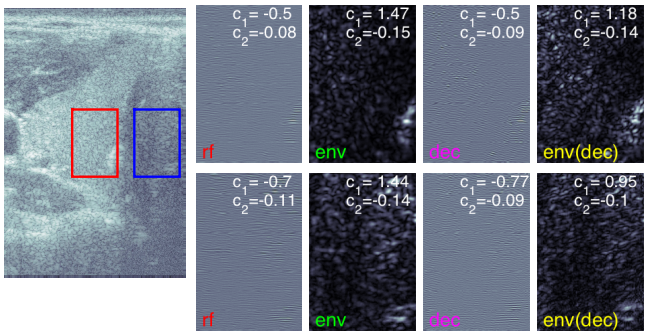


(a) (b) (c) (d) (e)

**Fig. 4**. **Results for real data.** Thyroid image (a, B-mode image) and rf (b), env (c), dec (d), env(dec) (e) images of red (top row) and blue (bottom row) patch, with estimates $c_1$, $c_2$.

tion. Therefore, while values for $c_1$ are different for the two patches and thus suggest a change in tissue properties, it can not be directly interpreted as a change in tissue fractality.

## 5. CONCLUSION AND PERSPECTIVES

This paper studied the influence of deconvolution on the estimation of tissue fractal and multifractal properties in US imaging. A simulation pipeline was proposed allowing to generate US images from tissues with available multifractal ground truth. Simulation results showed a better correlation between this ground truth and the estimated fractal and multifractal behavior from restored TRF than those estimated from native US data. These encouraging results open several perspectives including the consideration of other regularization than the $\ell_1$-norm, pursuing with more realistic simulation and the analysis of further *in vivo* data.

## 6. REFERENCES


[1] A. L. Coila and R. Lavarello, "Regularized spectral log difference technique for ultrasonic attenuation imaging," *IEEE T. Ultrasonics, Ferroelect., and Frequency Control*, vol. 65, no. 3, pp. 378–389, March 2018.

[2] M. L. Oelze and J. Mamou, "Review of quantitative ultrasound: Envelope statistics and backscatter coefficient imaging and contributions to diagnostic ultrasound," *IEEE T. Ultrasonics, Ferroelect., and Frequency Control*, vol. 63, no. 2, pp. 336–351, Feb 2016.

[3] M. A. Mohammed, B. Al-Khateeb, A. N. Rashid, D. A. Ibrahim, M. K. A. Ghani, and S. A. Mostafa, "Neural network and multi-fractal dimension features for breast cancer classification from ultrasound images," *Computers & Electrical Eng.*, vol. 70, pp. 871 – 882, 2018.

[4] E. Villain, H. Wendt, A. Basarab, and D. Kouamé, "On multifractal tissue characterization in ultrasound imaging," in *Proc. IEEE Int. Symp. Biomed. Imag. (ISBI)*, Venice, Italy, April 2019.

[5] H. Wendt, P. Abry, and S. Jaffard, "Bootstrap for empirical multifractal analysis," *IEEE Signal Processing Magazine*, vol. 24, no. 4, pp. 38–48, 2007.

[6] H. Wendt, S. G. Roux, P. Abry, and S. Jaffard, "Wavelet leaders and bootstrap for multifractal analysis of images," *Signal Processing*, vol. 89, no. 6, pp. 1100–1114, 2009.

[7] M. Alessandrini, S. Maggio, J. Poree, L. De Marchi, N. Speciale, E. Franceschini, O. Bernard, and O. Basset, "A restoration framework for ultrasonic tissue characterization," *IEEE T. Ultrasonics, Ferroelec. & Frequency Control*, vol. 58, no. 11, pp. 2344–2360, 2011.

[8] N. Zhao, A. Basarab, D. Kouamé, and J.-Y. Tourneret, "Joint Segmentation and Deconvolution of Ultrasound Images Using a Hierarchical Bayesian Model based on Generalized Gaussian Priors," *IEEE T. Image Proces.*, vol. 25, no. 8, pp. 3736–3750, 2016.

[9] S. Boyd, N. Parikh, E. Chu, B. Peleato, and J. Eckstein, "Distributed optimization and statistical learning via the alternating direction method of multipliers," *Foundations and Trends in Machine Learning*, vol. 3, no. 1, pp. 1–122, 2011.

[10] S. Mallat, *A Wavelet Tour of Signal Processing*, 3rd ed. Academic Press, 2008.

[11] E. Bacry, J. Delour, and J.-F. Muzy, "Multifractal random walk," *Phys. Rev. E*, vol. 64: 026103, 2001.

[12] L. Chevillard, R. Robert, and V. Vargas, "A stochastic representation of the local structure of turbulence," *Europhysics Letters*, vol. 89, p. 54002, March 2010.

[13] J. A. Jensen and N. B. Svendsen, "Calculation of pressure fields from arbitrarily shaped, apodized, and excited ultrasound transducers," *IEEE T. Ultrasonics, Ferroelec. & Frequency Control*, vol. 39, no. 2, pp. 262–267, March 1992.